Monthly Notices of the ROYAL ASTRONOMICAL SOCIETY

MNRAS **505,** 116–125 (2021) doi:10.1093/mnras/stab1369
Advance Access publication 2021 May 13

Enormous explosion energy of Type IIP SN 2017gmr with bipolar ^{56}Ni ejecta

Victor P. Utrobin [1,2,3★] Nikolai N. Chugai,[2★] Jennifer E. Andrews,[4★] Nathan Smith [4] Jacob Jencson,[4] D. Andrew Howell,[5,6] Jamison Burke,[5,6] Daichi Hiramatsu,[5,6] Curtis McCully[5,6] and K. Azalee Bostroem[7]

[1]*NRC 'Kurchatov Institute' – Institute for Theoretical and Experimental Physics, B. Cheremushkinskaya St. 25, 117218 Moscow, Russia*
[2]*Institute of Astronomy, Russian Academy of Sciences, Pyatnitskaya St. 48, 119017 Moscow, Russia*
[3]*Max-Planck-Institut für Astrophysik, Karl-Schwarzschild-Str. 1, D-85748 Garching, Germany*
[4]*Steward Observatory, University of Arizona, 933 North Cherry Avenue, Tucson, AZ 85721-0065, USA*
[5]*Department of Physics, University of California, Santa Barbara, CA 93106-9530, USA*
[6]*Las Cumbres Observatory, 6740 Cortona Dr, Suite 102, Goleta, CA 93117-5575, USA*
[7]*Department of Physics and Astronomy, University of California, 1 Shields Avenue, Davis, CA 95616-5270, USA*

Accepted 2021 May 9. Received 2021 April 19; in original form 2021 March 1

ABSTRACT

The unusual Type IIP SN 2017gmr is revisited in order to pinpoint the origin of its anomalous features, including the peculiar light curve after about 100 d. The hydrodynamic modelling suggests the enormous explosion energy of $\approx 10^{52}$ erg. We find that the light curve with the prolonged plateau/tail transition can be reproduced either in the model with a high hydrogen abundance in the inner ejecta and a large amount of radioactive ^{56}Ni, or in the model with an additional central energy source associated with the fallback/magnetar interaction in the propeller regime. The asymmetry of the late H α emission and the reported linear polarization are reproduced by the model of the bipolar ^{56}Ni ejecta. The similar bipolar structure of the oxygen distribution is responsible for the two-horn structure of the [O I] 6360, 6364 Å emission. The bipolar ^{56}Ni structure along with the high explosion energy are indicative of the magneto-rotational explosion. We identify narrow high-velocity absorption features in H α and He I 10 830 Å lines with their origin in the fragmented cold dense shell formed due to the outer ejecta deceleration in a confined circumstellar shell.

Key words: hydrodynamics – methods: numerical – supernovae: general – supernovae: individual: SN 2017gmr.

1 INTRODUCTION

Type IIP supernovae (SNe IIP) originate from a core collapse of massive stars ($>9\,M_\odot$) that retain a significant fraction of the hydrogen envelope until the explosion. The general paradigm is that the SN IIP light curve at the plateau stage is maintained by the release of the internal energy deposited during the propagation of the shock wave through the pre-SN envelope (Grassberg, Imshennik & Nadyozhin 1971), whereas the luminosity tail is powered by the radioactive decay $^{56}\mathrm{Co} \rightarrow {}^{56}\mathrm{Fe}$ (Weaver & Woosley 1980). The debatable explosion mechanisms of SNe IIP or, in a broad sense, of core-collapse SNe include the neutrino-driven explosion (Colgate & White 1966; Janka 2017; Burrows & Vartanyan 2021), the magneto-rotational explosion related to the magnetar formation (LeBlanc & Wilson 1970; Bisnovatyi-Kogan 1971; Khokhlov et al. 1999), and the jet-powered SNe related to the collapsar (rotating black hole plus disc) formation (MacFadyen, Woosley & Heger 2001).

In most observed cases, one cannot distinguish between different options, because the outcome of the SN explosion with the typical energy of $\sim 10^{51}$ erg is not sensitive to the explosion mechanism. An exception is the case when the explosion energy inferred from the hydrodynamic modelling significantly exceeds the upper limit for the neutrino-driven mechanism $E_{\rm up} \approx 2 \times 10^{51}$ erg (Janka 2017). Among 11 SNe IIP explored so far via the uniform hydrodynamic modelling (cf. Utrobin & Chugai 2019), only two events can be attributed to the category of high-energy SNe IIP with $E > E_{\rm up}$: SN 2009kf with $E = 2.15 \times 10^{52}$ erg (Utrobin, Chugai & Botticella 2010) and SN 2000cb with $E = 4.4 \times 10^{51}$ erg (Utrobin & Chugai 2011).

The recent SN IIP 2017gmr is another candidate for high-energy SNe IIP because it exhibits both high luminosity and high expansion velocities (Andrews et al. 2019). The hydrodynamic modelling of SN 2017gmr (Goldberg & Bildsten 2020) prefers a high explosion energy of $\approx 5 \times 10^{51}$ erg despite of the claimed model degeneracy with respect to SN parameters. It is noteworthy that SN 2017gmr shows signatures of asymmetry in the H α and [O I] 6360, 6364 Å emission lines on day 312 (Andrews et al. 2019) and in the polarization (Nagao et al. 2019), which indicate a non-spherical explosion.

Even more remarkable feature of SN 2017gmr is a steeper luminosity decline of the post-plateau tail compared to the ^{56}Co decay luminosity (Andrews et al. 2019). The hydrodynamic modelling of Goldberg & Bildsten (2020) is unable to account for this behaviour that is interpreted as an excess in the observed luminosity over the computed luminosity at the radioactive tail. Possible explanations for the fast tail decline include the early escape of gamma-quanta due to

★ E-mail: utrobin@itep.ru (VPU); nchugai@inasan.ru (NNC); jandrews@as.arizona.edu (JEA)

the decay of the radioactive ^{56}Co, the circumstellar (CS) interaction, or the early dust formation (Andrews et al. 2019), although the latter seems unlikely because of the high gas temperature at this stage. The CS interaction might be relevant, since early spectra show the narrow Hα emission with broad wings indicating the dense CS shell. Another possibility might be the high velocity of radioactive ^{56}Ni, favouring the early escape of the gamma rays similar to the case of SN 2013ej (Utrobin & Chugai 2017). The applicability of this conjecture for SN 2017gmr at the moment is unclear and must be examined.

Here we address unusual features of SN 2017gmr with an emphasis on the fast decline of the luminosity tail. To this end we revisit the construction of the bolometric light curve (Section 2) and then perform the hydrodynamic modelling and examine a number of possibilities for the origin of the fast tail decline (Section 3). The asymmetry effects in emission lines at the nebular stage and the polarization are explored in order to constrain the extent of mixing of radioactive ^{56}Ni (Section 4). We then address the effects of the CS interaction at the photospheric stage (Section 5). Finally, results are summarized and discussed in Section 6.

Below we adopt the distance of 19.6 Mpc and the reddening of $A(B-V) = 0.3$ mag (Andrews et al. 2019). The explosion date is set to be 2017 September 1.88, MJD 57997.89, which is recovered from the fit of the earliest r magnitudes by the hydrodynamic modelling. This moment is 1.20 d earlier compared to that adopted by Andrews et al. (2019).

2 BOLOMETRIC LIGHT CURVE AND PHOTOSPHERIC VELOCITIES

Additional late-time photometry presented here and not published in Andrews et al. (2019) was obtained via the Las Cumbres Observatory 1-m telescope network (Brown et al. 2013) with the Sinistro cameras in the framework of the Global Supernova Project. The data were reduced using the Beautiful Algorithms to Normalize Zillions of Astronomical Images (BANZAI) pipeline (McCully et al. 2018). PSF-fitting photometry was then performed using LCOGTSNPIPE (Valenti et al. 2016), a PYRAF-based photometric reduction pipeline. *UBV*-band data were calibrated to Vega magnitudes (Stetson 2000) using standard fields observed on the same night with the same telescope, while *gri*-band data were calibrated to AB magnitudes using the Sloan Digital Sky Survey (SDSS Collaboration; Albareti et al. 2017).

As described in Andrews et al. (2019), a quasi-bolometric light curve was created using the routine SUPERBOL (Nicholl 2018), where the reddening and redshift corrected photometry in each band (from *UV* to *IR*) was interpolated with the g band as reference, then converted into a spectral luminosity (L_λ). The bolometric luminosity was then computed from the integration of the SED for each epoch. While uncertainties in the reddening ($E(B-V) = 0.30 \pm 0.06$ mag) and distance (19.6 $\pm$ 1.4 Mpc) introduce uncertainties in the total bolometric luminosity, the bolometric light curve falls much more rapidly than expected for a fully-trapped ^{56}Co decay.

To get an idea of the late-time ($t > 170$ d) bolometric luminosity, we convert V magnitudes into bolometric fluxes using a relation between V and bolometric magnitudes for SN 1987A (Catchpole et al. 1988; Whitelock et al. 1988). This procedure suggests that spectral energy distributions of SN 2017gmr and SN 1987A are similar and differ only by a constant factor that can be fixed by matching bolometric luminosities of SN 2017gmr around day 170 (Fig. 1).

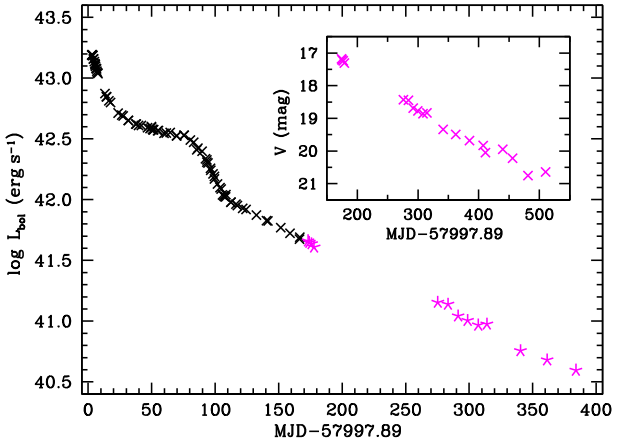

Figure 1. Bolometric light curve integrated from NUV to NIR with blackbody corrections (grey crosses) and the late-time reconstruction based on V magnitudes (magenta asterisks). The inset shows late-time V magnitudes.

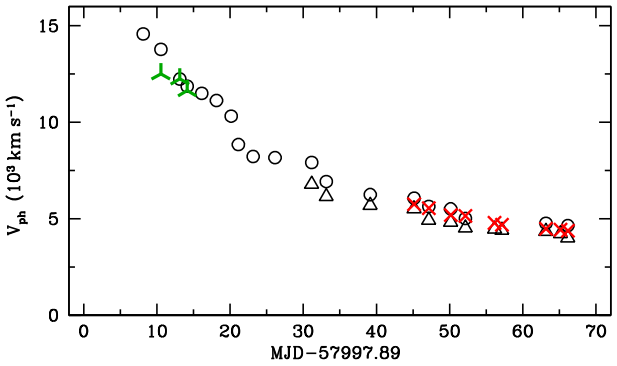

Figure 2. Velocity at the photosphere level of SN 2017gmr inferred from absorption minima of four lines: H β (black circles), He I 5876 Å (green three point star symbols), Fe II 5169 Å (black triangles), and Na I 5892 Å doublet (red crosses).

The velocities at the photosphere (Fig. 2) are estimated from absorption minima of H β, Fe II 5169 Å, He I 5876 Å, and Na I 5892 Å doublet in spectra of SN 2017gmr (Andrews et al. 2019). In the case of Na I, we treat photon scatterings in the doublet by the Monte Carlo technique to recover the photospheric velocity from the absorption minimum. According to the Fe II 5169 Å absorption the photospheric velocity is lower by $\sim$500 km s^{-1} compared to the velocities from H β and Na I 5892 Å doublet (Fig. 2). The possible reason for that might be the presence of Mg I 5167 Å, 5173 Å, 5184 Å triplet. The optical depth of the strongest triplet line Mg I 5184 Å is comparable to that of Fe II 5169 Å for the ionization fraction Mg I/Mg of $\sim$0.025. We performed Monte Carlo simulations of the radiation transfer for the blend of Fe II and Mg I triplet assuming that the Sobolev optical depth of the strongest Mg I line 5184 Å line is equal to that of the Fe II 5169 Å line. The absorption minimum in this case turns out shifted towards red by about 500 km s^{-1}, which could explain the lower velocity according to the Fe II 5169 Å line.

Noteworthy, the radial velocity of an absorption minimum ($|v_{\rm min}|$) of the P Cygni profile may differ from the photospheric velocity ($v_{\rm ph}$). The equality $|v_{\rm min}| = v_{\rm ph}$ takes place only for the scattering lines of a moderate strength. For a strong line, even with the conservative scattering, the minimum is displaced towards blue due to the scattered emission, so in this case, $|v_{\rm min}| > v_{\rm ph}$. This effect is strengthened by a net emission likewise in the case of Hα. For a weak absorption,

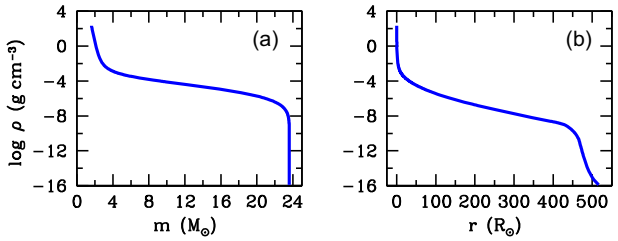

Figure 3. Density distribution as a function of interior mass (panel a) and radius (panel b) for the pre-SN model HM-optm (Table 1). The central core of 1.6 $M_\odot$ is omitted.

in contrast, $|v_{min}| < v_{ph}$, because, in this case, the absorption is formed by a narrow layer close to the photosphere and projection effects shift the absorption minimum towards zero radial velocity. We therefore admit that the velocity recovered from the shallow H β and He I absorptions at the early stage ($t < 20$ d) likely underestimate the photospheric velocity by about 20 per cent. At the later stage ($t > 20$ d), the H β absorption is moderately strong and the net and scattered emissions are suppressed because of the H β quanta conversion into P α and H α. We thus believe that the H β absorption provides a reliable measure of the photospheric velocity at this stage.

3 HYDRODYNAMIC MODELLING

3.1 Model overview

To hydrodynamically model the SN IIP 2017gmr, we use the time-implicit Lagrangian radiation hydrodynamics code CRAB that integrates the set of spherically symmetric hydrodynamic equations including self-gravity, and a radiation transfer equation in the grey approximation (Utrobin 2004, 2007). The explosion of the pre-SN model is initiated by a supersonic piston applied to the stellar envelope at the boundary with the collapsing 1.6-$M_\odot$ core. The pre-SN model is the hydrostatic non-evolutionary model of a red supergiant (RSG) star. It should be emphasized that the choice of the non-evolutionary model is motivated by the following arguments. First, the description of the light curve and photospheric velocities of SNe IIP by the spherically symmetric hydrodynamics cannot be attained based on the current evolutionary pre-SN models (Utrobin & Chugai 2008): the modification of the density distribution of the hydrogen envelope and the smoothing density and composition gradients at the metals/He and He/H composition interfaces is needed. Secondly, the RSG explosion in three-dimensional (3D) hydrodynamic simulations indeed results in smoothing the density and composition gradients at the metals/He and He/H composition interfaces (Utrobin et al. 2017). Third, at the final stage of the pre-SN evolution, the density distribution in the hydrogen envelope can be modified by the acoustic waves excited by the vigorous convection at the Ne-burning stage (Shiode & Quataert 2014). These arguments unavoidably compels us to choose a non-evolutionary RSG model in which the structure modification can be implemented by hand to make the spherically symmetric hydrodynamic model appropriate for the description of the observational data (Figs 3 and 4). It is noteworthy that the hydrogen abundance in the inner layers of the mixed ejecta $X_c \approx 0.05$ is comparable to the value of about 0.03 produced by the 3D hydrodynamic model of SN 1999em (Utrobin et al. 2017). However, mixing induced by the SN explosion can be affected by particular features of the explosion mechanism, e.g. explosion asymmetry, so the higher hydrogen abundance in the central zone of the expanding ejecta cannot be ruled out.

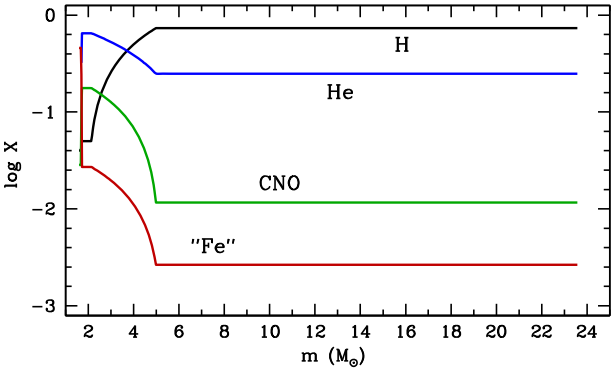

Figure 4. Mass fractions of major constituents: hydrogen (black line), helium (blue line), CNO elements (green line), and Fe-peak elements without radioactive ^{56}Ni (red line) in the ejected envelope of model HM-optm (Table 1).

Table 1. Basic properties of hydrodynamic models[a].

Model	M_{ej} ($M_\odot$)	E (10^{51} erg)	M_{Ni} ($M_\odot$)	v_{Ni}^{max} (km s^{-1})	X_c	Note
HM-refm	22.0	10.2	0.16	3300	0.05	Reference
HM-hmix	22.0	10.2	0.18	3300	0.20	H mixing
HM-lmas	14.0	10.0	0.20	3400	0.04	Low M_{ej}
HM-exni	22.0	10.2	0.23	7900	0.05	Outer ^{56}Ni
HM-magn	22.0	10.2	0.01	3300	0.05	Magnetar
HM-optm	22.0	10.2	0.11	3300	0.05	FM-mechanism

[a] In all models, the pre-SN radius R_0 is 525 $R_\odot$.

We do not solve the complicated optimization problem to construct the optimal pre-SN model; instead, we rely on the well-studied effects of model parameters on the light curve and the photospheric velocity (e.g. Grassberg et al. 1971; Woosley 1988; Utrobin 2007). The optimal pre-SN model that reproduces the major observational data of SN 2017gmr (i.e. the light curve and the evolution of the photospheric velocity) is found by means of hydrodynamic simulations for an extended set of SN parameters and a several options for the energy source at the plateau/tail transition, the distribution of radioactive ^{56}Ni being fixed by the nebular spectra.

Along with the pre-SN radius, the ejecta mass, the explosion energy, and the total amount of radioactive ^{56}Ni, the extent of its mixing in velocity space affects the light curve at the plateau as well. For SN 2017gmr, the extent of ^{56}Ni mixing is constrained by the H α emission on day 312 (Section 4). We find that the outer boundary of ^{56}Ni ejecta should lie at about 3300 km s^{-1} in the freely expanding envelope. The overall density and ^{56}Ni distribution in the ejecta on day 50 for model HM-optm (Table 1) is shown in Fig. 5. Note that in the broad range of expansion velocities $6000 < v < 30\,000$ km s^{-1}, the density distribution follows the power law $\rho \propto v^{-8}$.

3.2 Plateau/tail transition and luminosity tail

The hydrodynamic modelling leads us to the reference model HM-refm (Table 1) that fits in general the initial luminosity peak, the plateau, the late-time radioactive tail, and the photospheric velocities of SN 2017gmr (Fig. 6). However, this model demonstrates the essential deficit in the luminosity at the plateau/tail transition in the range of 90–140 d. The impression is that the plateau/tail transition of SN 2017gmr is overlong compared to ordinary SNe IIP. Note that the recent hydrodynamic modelling of SN 2017gmr by Goldberg &

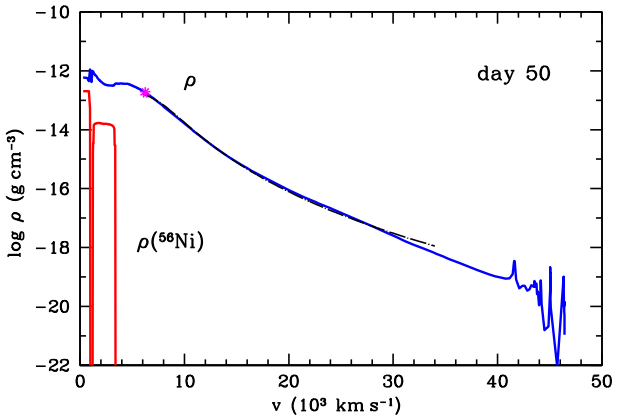

Figure 5. The gas (blue line) and ^{56}Ni (red line) density as a function of velocity on day 50 for model HM-optm (Table 1). Magenta star indicates the position of the photosphere. The dash–dotted line is the power law $\rho \propto v^{-8}$.

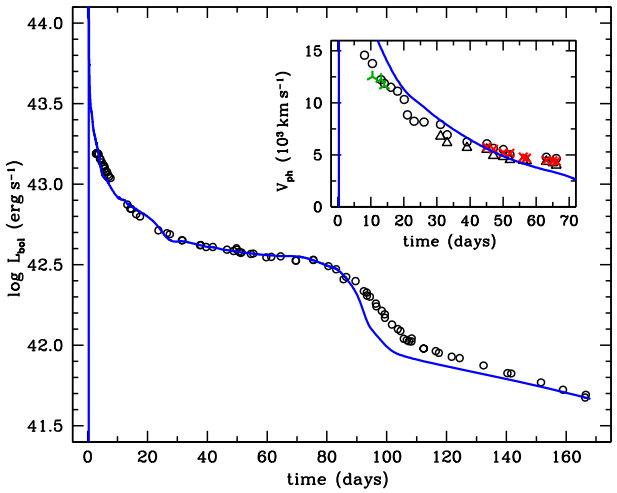

Figure 6. The bolometric light curve of model HM-refm (blue line, Table 1) overplotted on the observational data (black circles). Time is measured in days from core collapse. Inset shows the evolution of model velocity at the photosphere level defined by the effective optical depth of 2/3 (blue line) compared to the photospheric velocities estimated from the H β, He I 5876 Å, and Fe II 5169 Å lines and the Na I 5892 Å doublet. See Section 2 and the caption of Fig. 2 for details.

Bildsten (2020) faces the same problem of the model drawback at the plateau/tail transition.

Increasing both the total amount of radioactive ^{56}Ni and the opacity of the inner layers of the ejecta might compensate for the luminosity deficit. The higher opacity could be related to a more intense inward mixing of hydrogen-rich matter as a result of a strong explosion asymmetry compared to ordinary SNe IIP. The study of this possibility results in model HM-hmix (Table 1) whose ^{56}Ni mass of 0.182 $M_\odot$ and hydrogen abundance in the central zone $X_c = 0.2$ are larger than 0.158 $M_\odot$ and $X_c = 0.05$ of the reference model, respectively. The excellent fit to the observations in the range $t \leq 130$ d lends credibility to this model, although the later steep tail decline is not fully reproduced (Fig. 7).

Among other possibilities to resolve the issue of the steep luminosity tail, one can admit the low ejecta mass that favours a more efficient escape of gamma rays from the ^{56}Co decay. The appropriate low-mass model HM-lmas (Table 1) that fits the tail requires the

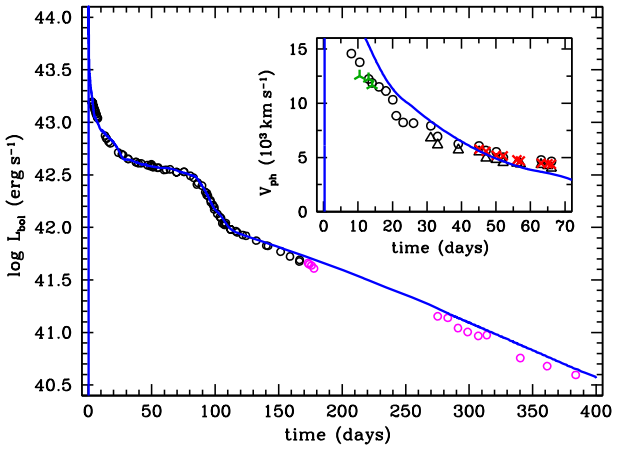

Figure 7. The bolometric light curve of model HM-hmix with the enhanced hydrogen abundance in the central zone of the ejecta (blue line, Table 1) overplotted on the observational data. Inset shows the evolution of model velocity at the photosphere level. See the caption of Fig. 6 for details.

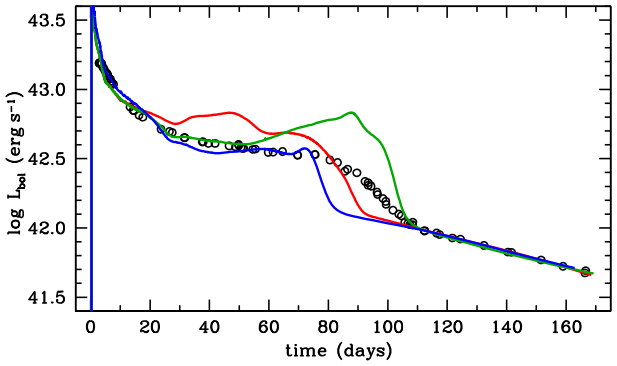

Figure 8. The bolometric light curves of three models (Table 1) that are able to reproduce the observed luminosity tail: model HM-lmas with the low ejecta mass (blue line), model HM-exni with the external ^{56}Ni (red line), and model HM-magn with the standard magnetar luminosity (green line).

ejecta mass of 14 $M_\odot$ with the ^{56}Ni mass of 0.2 $M_\odot$ (Fig. 8, blue line). This model, expectedly, produces too short plateau and should be rejected.

Another possibility is prompted by the model with the external ^{56}Ni ejecta that was successfully applied to SN 2013ej (Utrobin & Chugai 2017). The similar hydrodynamic model HM-exni (Table 1) for SN 2017gmr with the external ^{56}Ni fits the radioactive tail (Fig. 8, red line), if all the 0.23 $M_\odot$ of ^{56}Ni resides in the velocity range of 6000–8000 km s^{-1}. The drawback of this model is a pronounce luminosity excess at the plateau in the interval of 30–80 d and the luminosity deficit at the plateau/tail transition. The external ^{56}Ni thus cannot resolve the problems of the anomalous light curve of SN 2017gmr.

One can consider somewhat exotic model HM-magn in which the magnetar, not radiative ^{56}Ni, determines the luminosity tail. With a standard magnetar luminosity evolution $L = L_0/(1 + t/t_0)^2$, the tail can be described with the following parameter values: $L_0 = 4.47 \times 10^{43}$ erg s^{-1} and $t_0 = 19.07$ d. The rest of model parameters are in Table 1. The apparent drawback of the magnetar model is a large luminosity excess at the end of the plateau (Fig. 8, green line). The magnetar model in a simple version thus cannot resolve

simultaneously the issue of the plateau/tail transition and of the steep luminosity tail.

We briefly address a possible role of the CS interaction. Although this mechanism potentially is able to provide the steep luminosity tail; however, in this case it is highly unlikely. The point is that the interaction power of $\sim 10^{42}$ erg s^{-1} required at about 100 d is released in the outer layers of the ejecta that would be inevitably accompanied by a strong broad Hα emission with the luminosity of $\sim 10^{41}$ erg s^{-1} and a specific line profile lacking the absorption component. This is not the case for SN 2017gmr (cf. Andrews et al. 2019), so the significant contribution of the spherical CS interaction is ruled out. To overcome this problem, one might admit that the CS matter is arranged in the form of a dense equatorial ring that is overtaken by the SN envelope (e.g. Chugai & Danziger 1994; Smith et al. 2015). In that case one expects that the forward and reverse shocks are submerged inside the envelope, so the released radiation creates a quasi-spherical photosphere. This scenario, however, should reveal strong effects of the non-spherical interaction in the early Hα profile. Instead, the spectra show the usual steady evolution – a characteristic of spherical SNe IIP. The CS interaction as a major energy source at the early luminosity tail thus should be rejected.

3.3 Central energy source?

An interesting possibility to resolve the issue of the post-plateau light curve involves an additional energy source related to the fallback on the magnetar. The conjecture looks quite sensible by two reasons: First, the fallback accretion flow always accompanies the core-collapse SNe (Colgate 1971; Chevalier 1989), and second, the magnetar formation could be a natural outcome of the magneto-rotational explosion mechanism that is required to provide the enormous explosion energy of $\sim 10^{52}$ erg. The extra energy source involving both the fallback and the magnetar we dub 'FM-mechanism', for short. The dense environment associated with the fallback inhibits the magnetic dipole radiation of the magnetar, whereas the FM-mechanism could release rotational energy in the propeller regime that operates when the Alfven radius $R_{\rm m}$ exceeds the corotation radius $R_{\rm c}$ and both of these radii are less than the radius of the light cylinder (Illarionov & Sunyaev 1975; Shakura 1975). Conditions required for the FM-mechanism to operate successfully can be illustrated by the case of the unusual SN ASASSN-15nx with the luminosity decreasing in the range of 5×10^{42} to 5×10^{41} erg s^{-1} between days 100 and 200 (Chugai 2019). In that case the light curve has been modelled in terms of the FM-mechanism assuming a spherical fallback with the accretion rate $\dot{M} \sim 10^{-3}\,{\rm M}_\odot\,{\rm yr}^{-1}$ on to the magnetosphere of the neutron star with the magnetic momentum $\mu \sim 5 \times 10^{31}\,{\rm G\,cm}^3$, and the rotation period $p \sim 10^{-2}$ s. These values could be applicable for the FM-mechanism in the case of SN 2017gmr, although some complications could arise due to the unknown specific angular momentum of the fallback material.

We will constrain the rate of the power release by the FM-mechanism, $L_{\rm c}(t)$, using the hydrodynamic modelling. To this end we impose the power $L_{\rm c}(t)$ at the inner boundary of the computational domain immediately after the explosion. The model HM-optm (Table 1) with the ^{56}Ni mass of 0.11 M$_\odot$ reproduces both the observed plateau/tail transition and the luminosity tail decline (Fig. 9) for the adopted luminosity $L_{\rm c}(t)$ shown in the same plot. The required evolution of the additional energy source is characterized by a slow rise towards the maximum at about 80 d and an exponential decline later on. In fact, the exponential behaviour is constrained only to the stage of $t < 180$ d; we retain the later exponential behaviour simply to minimize a number of parameters, although the preferred option

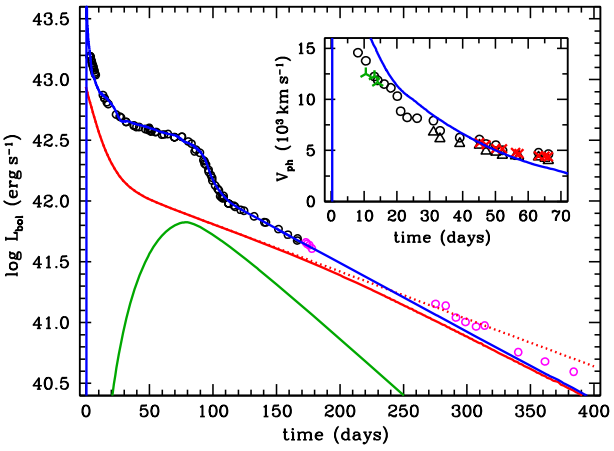

Figure 9. The bolometric light curve of model HM-optm (blue line, Table 1) overplotted on the observational data (black and magenta circles). A good fit to the observations is obtained with the additional energy source applied to the internal boundary of the ejecta (green line) and the energy deposition of gamma rays by radioactive decay of ^{56}Ni (solid red line). The dotted red line shows the total power of the radioactive decay. The inset shows the evolution of the photospheric velocity in the same way as in Fig. 6.

is zero contribution of the extra energy source to the luminosity on day 312.

At first glance, the adopted luminosity evolution of the FM-mechanism looks highly artificial. In fact, it is not, because the fallback accretion rate at the early stage is high enough to shrink the magnetosphere so strongly that the inequality $R_{\rm m} < R_{\rm c}$ is fulfilled thus turning off the propeller regime. In this case, the gravitational energy of the fallback accretion flow is released in the close vicinity of neutron star producing the neutrino luminosity (Chevalier 1989).

It should be emphasized that the conjecture about the extra energy source is viable so long as the conclusion on the fast decline of the observed luminosity tail remains valid.

3.4 Constraining the ejecta mass

The adequate hydrodynamic model is constructed by fitting the photometric and spectroscopic observations of the object under study. The important physical parameters – the initial radius R_0, the ejecta mass $M_{\rm ej}$, and the explosion energy E – can be reliably estimated from the detailed observations of the whole outburst, particularly, at both the shock breakout and the plateau/tail transition. Photometric data of SN 2017gmr are well defined at both epochs and are sufficiently comprehensive to construct the bolometric light curve (Andrews et al. 2019). The rising part of the r-band light curve after the shock breakout is strengthened by the upper limit in the r band obtained 2 d before the SN discovery (Andrews et al. 2019) in constraining the basic parameters of hydrodynamic model.

Model HM-optm excellently fits the early $M_{\rm r}$ magnitudes and satisfies the upper limit provided the explosion occurs at MJD 57997.89 (Fig. 10). It is noteworthy that during the first several days the SN spectrum is essentially the Planck function that permits us to adequately calculate the r-band magnitude with the radiation hydrodynamics code CRAB. Interestingly, the flux in the r band shows a double peak structure that is, to our knowledge, has never been noticed either observationally or numerically. In this particular model the double peak phenomenon is related to the formation of the opaque thin dense shell at about 0.38 d after the collapse and $\sim$1 h after the shock breakout due to the sweeping of the external

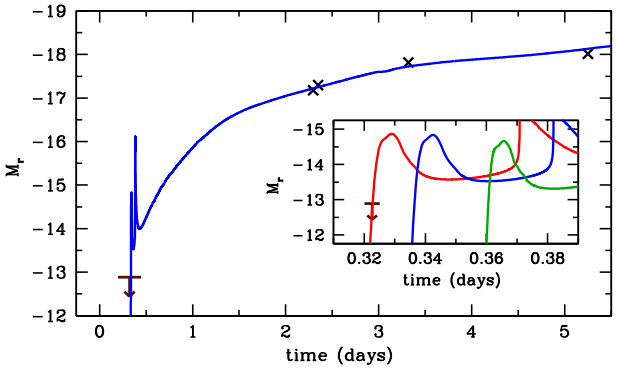

Figure 10. Rising part of the *r*-band light curve during the first 5.5 d for model HM-optm (blue line) compared to observational data (Andrews et al. 2019, black crosses). The brown arrow shows the observational upper limit taken by Andrews et al. (2019) about 2 d prior to SN discovery. Inset shows sensitivity of the rising part of the *r*-band light curve for the models with different ejecta masses at E/M_{ej} = const: model with M_{ej} = 21 $M_\odot$(red line), model HM-optm with M_{ej} = 22 $M_\odot$(blue line), and model with M_{ej} = 24 $M_\odot$(green line). The model with M_{ej} = 21 $M_\odot$imposes the lower limit of the ejecta mass (Section 3.4).

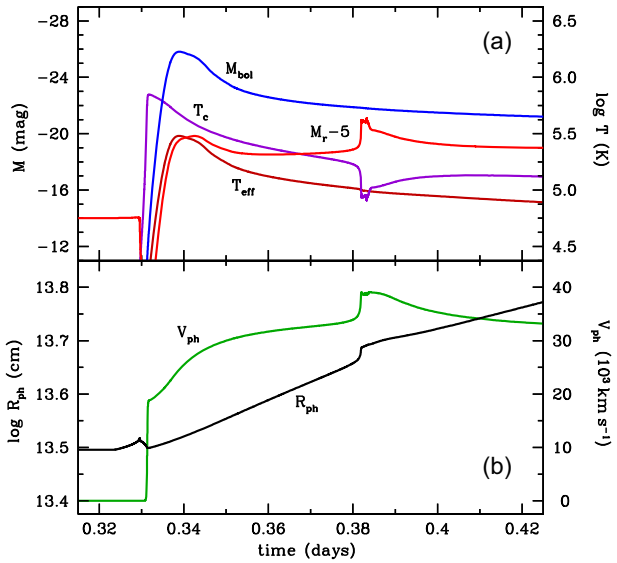

Figure 11. The physics of the double peak structure in the *r*-band maximum occurring during the first 2 h after the shock breakout. Panel (a): The first maximum in the *r*-band light curve (red line) at $t \sim 0.34$ d is related to the maximum of the bolometric luminosity (blue line), while the second maximum at $t \sim 0.38$ d is related to the formation of the thin shell accompanied by the drop of the colour temperature (magenta line). Note that both the bolometric luminosity and the effective temperature (Indian red line) monotonically decrease around the second maximum. Panel (b): The behaviour of the photospheric radius (black line) and velocity (green line) in the vicinity of the second maximum reflects the thin shell formation.

layers into the thin shell by the pressure of the escaping radiation flux. To illustrate the point we show the evolution of related values, viz., the absolute bolometric magnitude M_{bol}, the absolute *r*-band magnitude M_r, the effective temperature T_{eff}, the colour temperature T_c, the photospheric velocity v_{ph}, and the photospheric radius R_{ph} (Fig. 11). It is noteworthy that the *r*-band flux shows a jump at ∼1 h after the shock breakout, whereas the bolometric flux does not. This suggests that the variation of the *r*-band flux is essentially related to

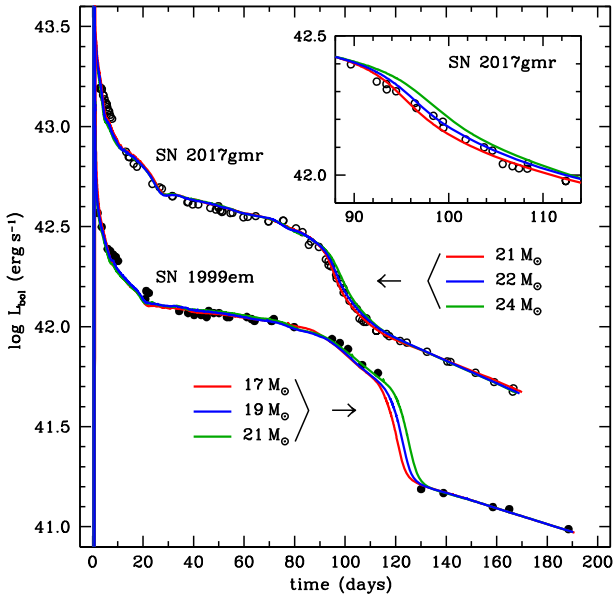

Figure 12. Sensitivity of the bolometric light curve to the ejecta mass variation at E/M_{ej} = const for SN 1999em and SN 2017gmr. The bolometric light curve of SN 1999em was taken from Elmhamdi et al. (2003). In the case of SN 2017gmr, the sensitivity to the mass variation is relatively weak because the plateau/tail transition is affected by the additional luminosity of the central source. Inset shows that even in this case the models with different ejecta masses are clearly distinguished.

that in the colour temperature (Fig. 11a). The formation of the thin opaque shell is accompanied by its radiative acceleration clearly seen in the behaviour of the velocity at the photosphere (Fig. 11b). The double peak structure in the *r* (in other bands as well) light curve is an interesting phenomenon that could be used in future as an additional tool in order to constrain SN IIP parameters.

The plateau length t_p of hydrodynamic models of SNe IIP is known to be almost independent of the ejecta mass given the constant ratio E/M_{ej}. For example, in the case of the normal IIP SN 1999em, it shows only weak dependence on the explosion energy $t_p \propto E^{-0.18}$ and the pre-SN radius $t_p \propto R_0^{0.10}$ (Utrobin 2007). Such a behaviour of hydrodynamic models produces the impression of a degeneracy with respect to the model parameters. However, in the rigorous sense, the degeneracy on the ejecta mass is absent. We demonstrate this fact for SN 1999em with auxiliary hydrodynamic models in which E/M_{ej} = const and the calculated bolometric luminosity is secured at the observed plateau luminosity by the appropriate choice of the pre-SN radius. These models with the different ejecta masses deviated from the value of 19 $M_\odot$ by ±2 $M_\odot$ show significant difference at the plateau/tail transition (Fig. 12). This numerical experiment suggests that the distributions of the major elements and ^{56}Ni are fixed in the ejecta (Figs 4 and 5). Any variation of these distributions results in the deformation of the model light curve at the end of the plateau and the plateau/tail transition, which is inconsistent with observations. It is noteworthy that the uncertainty of the ejecta mass becomes significant (>10 per cent), if the date of the explosion is fixed with an error worse than ∼2 d.

In the special case of SN 2017gmr with the additional central energy source the dependence on the ejecta mass is weaker, yet even in this case we are able to distinguish between the models with the ejecta masses of 21, 22, and 24 $M_\odot$ (Fig. 12, inset). It is remarkable that the upper limit in *r*-band taken 2 d before the SN discovery imposes serious constraint on the ejecta mass. Its physical meaning

can be explained by the following reasonings. Using the approximate formulae relating the physical parameters to the observable properties of hydrodynamic models (Utrobin 2007) with $E/M_{\rm ej} = {\rm const}$ and the fixed bolometric luminosity at the plateau, we find that $R_0 \propto M_{\rm ej}^{-1.51}$. In other words, the lower the ejecta mass is, the larger the pre-SN radius, and, consequently, the larger the characteristic expansion time. The latter results in the longer time interval between the shock breakout and the epoch of the SN discovery at $M_{\rm r} = -17.18$ mag. This implies that there is a lower limit of the ejecta mass determined by the interval between the time of the upper limit in the r band and the discovery epoch. This interval is exactly realized in the hydrodynamic model with the ejecta mass of 21 $M_\odot$ (Fig. 10, inset). Model HM-optm with the ejecta mass of 22 $M_\odot$ excellently fits both the upper limit in r band and the early $M_{\rm r}$ magnitudes (Fig. 10), and the observed bolometric light curve as a whole (Fig. 9).

In addition to the lower limit of the ejecta mass of 21 $M_\odot$, we can estimate the uncertainty in the derived SN parameters by varying the model parameters around the optimal model. The uncertainty of 1.4 Mpc in the SN distance and the uncertainty of about 0.06 mag in the reddening $E(B-V)$ (Andrews et al. 2019) imply nearly 20 per cent uncertainty in the bolometric luminosity. The scatter in the plot of the photospheric velocity versus time (Fig. 9, inset) suggests the uncertainty of about 7 per cent in the photospheric velocity. We estimate the maximal uncertainty of the plateau length as 4 d, i.e. 4 per cent of the plateau duration. With these uncertainties of observables, we have the initial radius of $525 \pm 176\,R_\odot$, the ejecta mass of $22^{+2}_{-1}\,M_\odot$, the explosion energy of $(10.2 \pm 0.83) \times 10^{51}$ erg, and the total ^{56}Ni mass of $0.110 \pm 0.023\,M_\odot$.

4 ASYMMETRY OF ^{56}NI EJECTA

The triple-peaked Hα profile in the spectrum on day 312 (Andrews et al. 2019) suggests a non-spherical line-emitting region. Following a concept employed for the SN IIP 2004dj (Chugai et al. 2005), the SN IIP 2016X (Utrobin & Chugai 2019), and the SN II 2010jp (Smith et al. 2012), we attribute the Hα asymmetry to the bipolar ^{56}Ni ejecta embedded into a spherical envelope. For SN 2017gmr, the ^{56}Ni distribution is represented by three collinear homogeneous spheres: central, front, and rear. The radii, the shifts, and the masses of components are found via the fit of the Hα line profile for the optimal inclination angle. The latter is constrained by relying on the linear polarization $p = 0.37 \pm 0.04$ per cent on day 136 (Nagao et al. 2019). The density distribution in the envelope is set analytically as $\rho(v) = \rho_0 (v_0/v)^{0.5}/[1 + (v/v_0)^{7.5}]$ with ρ_0 and v_0 specified by the ejecta mass of 22 $M_\odot$ and the explosion energy of 10^{52} erg. The adopted density distribution in the outer layers $\rho \propto v^{-8}$ is well consistent with the hydrodynamic model HM-optm (Fig. 5).

The energy deposition by γ-rays is treated in a single flight approximation with the absorption coefficient $k_\gamma = 0.03(1+X)$ cm^2 g^{-1} (Kozma & Fransson 1992), where X is the hydrogen mass fraction assumed to be uniform in the ejecta. We adopt $X = 0.5$ to allow for the synthesized helium. Positrons from e^--capture channel deposit their kinetic energy on-the-spot. The ionization rate by the Compton and secondary electrons is calculated with the energy fractions spent on ionization, excitation, and heating according to Xu et al. (1992). The recombination rate corresponds to the total recombinations on levels $n > 2$ assuming the electron temperature of 5000 K. The adopted recombination regime approximately allows for the ionization from the second level by the recombination Balmer continuum and by the two-photon hydrogen continuum. The recombination Hα emissivity corresponds to case C (opaque Balmer lines), which implies that each recombination on to levels $n > 2$ ends up with the Hα quanta emission.

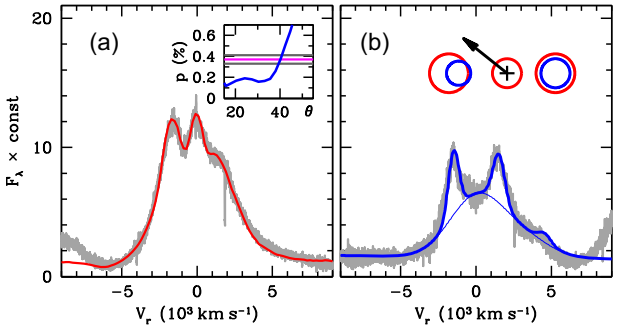

Figure 13. Asymmetry in the Hα and [O I] 6300, 6364 Å line profiles taken on day 312 (Andrews et al. 2019, grey lines). Panel (a): the model Hα line is given by red line. Inset shows the computed polarization as a function of inclination angle (blue line) and the observed polarization degree (horizontal magenta line) along with the $\pm\sigma$ lines (horizontal grey lines) (Nagao et al. 2019). Panel (b): thick blue line represents the resultant model [O I] 6300, 6364 Å line and thin blue line corresponds to the extended spherical emissivity component. Cartoon shows the spherical and bipolar components of the radioactive ^{56}Ni distribution (red circles) and the bipolar components of the [O I] emissivity (blue circles). Arrow indicates the direction towards observer.

Table 2. Parameters of ^{56}Ni components.

Component	$v_{\rm s}$	$v_{\rm r}$	$M_{\rm Ni}$
	(km s^{-1})		($M_\odot$)
Front	2400	900	0.059
Rear	2100	900	0.025
Central	0	700	0.026

The inclination angle is found using the iterative procedure starting with a certain ^{56}Ni configuration: ^{56}Ni $\rightarrow$ Hα $\rightarrow$ polarization $\rightarrow$ ^{56}Ni, etc. The polarization computation (Chugai 2006) is based on the Monte Carlo technique that follows the history of photons created by a central spherical source with a subsequent Thomson multiple scattering in the non-spherical distribution of electrons produced by the bipolar ^{56}Ni ejecta. The found inclination angle is $\theta = 40^\circ$ (Fig. 13a) with the radii $v_{\rm r}$, the shifts $v_{\rm s}$, and the masses of ^{56}Ni components given in Table 2. The bipolar components are not completely symmetrical: rear component has the lower bulk velocity and the lower mass compared to the front component. For the ^{56}Ni mass of 0.11 $M_\odot$, the model Hα luminosity of 3×10^{39} erg s^{-1} on day 312 coincides with the observed value of 3.2×10^{39} erg s^{-1} estimated from the flux-calibrated spectrum. This choice of the ^{56}Ni mass is consistent also with the light curve of model HM-optm (Fig. 9).

A reliable modelling of the thermal state of the [O I] doublet-emitting region is beyond reach given the significant role of the cooling by CO and SiO in the oxygen-rich matter (Liu & Dalgarno 1995). To get idea of the asymmetry of the oxygen line-emitting region, we decompose [O I] 6300, 6364 Å doublet using spherical Gaussian components, central, front, and rear, assuming the inclination angle of 40°. The components are specified by the normalized emissivity $j = A\exp[-(u/b)^2]$, where u is a velocity distance from the centre of the component with a certain velocity shift $v_{\rm s}$ (Table 3, Fig. 13b). The bipolar components of the oxygen emissivity in [O I] 6300, 6364 Å doublet are rather similar to those of ^{56}Ni (Fig. 13b, inset). This could be interpreted in two ways: either oxygen components reflect the distribution of the electron temperature due to the bipolar ^{56}Ni in a spherical oxygen-rich gas, or the oxygen ejecta have essentially

Table 3. Parameters of [O I] doublet components.

Component	v_s	b	A
	($km\,s^{-1}$)		
Front	2000	500	1.0
Rear	2000	600	0.3
Central	0	600	0.047

bipolar structure. The absence in the oxygen 6300 Å line narrow counterpart related to the central ^{56}Ni component favours the bipolar oxygen distribution.

A conjecture that the [O I] doublet originates from the toroidal oxygen distribution might be conceivable. However, the modelling shows that for any parameters, the toroidal structure fails to reproduce the observed [O I] doublet profile. The toroidal oxygen distribution is thus ruled out.

5 CIRCUMSTELLAR INTERACTION

The narrow Hα emission revealed by the early spectra of SN 2017gmr (Andrews et al. 2019) on days 1.5 and 2.3 and disappeared 3 d later suggests the presence of a dense confined CS shell similar to that of SN 2013fs (Yaron et al. 2017; Bullivant et al. 2018). The hydrodynamic interaction of the ejecta with the CS shell should result in the additional optical luminosity powered by the forward and reverse shocks. Another consequence of the CS interaction is the formation of a thin cold dense shell (CDS) between two shocks. The latter is observed in some SNe IIP as a narrow high-velocity ($\sim 10^4$ km s^{-1}) absorption (NHVA) in the Hα, He I 10 830 Å, and possibly Hβ lines at about 50–100 d (Chugai, Chevalier & Utrobin 2007). The optical and near-infrared spectra of SN 2017gmr indeed reveal distinctive NHVA in the Hα and He I 10 830 Å lines with velocities decreasing in the range 14 000–12 000 km s^{-1} between days 50 and 100. We identify this feature with the CDS partially fragmented due to Rayleigh–Taylor instability (Chugai et al. 2007). The manifestation of the CS interaction as the luminosity excess and the NHVA can be used to constrain the parameters of the SN ejecta and CS shell.

We treat the CS interaction based on a thin shell approximation (Chevalier 1982). The interaction model was described earlier (Chugai 2001) and here we recap only the essential points. The CDS dynamics is computed using Runge–Kutta fourth-order solver (Press et al. 2007). The shock radiative cooling time t_c at a certain moment is determined assuming the electron-ion equilibration with the post-shock density four times greater that the pre-shock density. This description is not valid at the very early stage, $t < 10$ h after the shock breakout, when the radiative precursor strongly accelerates the preshock gas thus diminishing the viscous shock. The forward and reverse shock luminosity is approximated as $L_k/(1 + t_c/t)$, where L_k is the shock kinetic luminosity. The interaction optical luminosity is equal to the X-ray luminosity absorbed by the unshocked ejecta and the CDS. The density of the homologously expanding ejecta is set as before $\rho = \rho_0(v_0/v)^{0.5}/[1 + (v/v_0)^{7.5}]$. The density distribution of the confined CS shell is adopted to be uniform in the range of $r < 5 \times 10^{14}$ cm with a drop $\rho \propto 1/r^4$ in the range of (1–2) $\times 10^{15}$ cm and the steady wind $\rho \propto 1/r^2$ in the outer zone $r > 2 \times 10^{15}$ cm (Fig. 14b, inset). The adopted CS shell extent is in line with that for SN 2013fs, (0.4–1) $\times 10^{15}$ cm (Yaron et al. 2017).

Our strategy is to find a model that minimizes the CS luminosity and meets the kinematic requirements imposed by the NHVA. The luminosity and the kinematic properties of the CDS depend on the CS density and the density $\rho(v)$ of the external layers of the SN ejecta. For a given ejecta mass of 22 M$_\odot$, the latter is determined by the explosion energy that can be found from the luminosity and the kinematic constraints. We find that the preferred explosion energy is of 6 $\times$ 10^{51} erg, whereas the mass of the confined CS shell is of 4 $\times$ 10^{-3} M$_\odot$. Remarkably, the latter value is comparable to the mass estimate for the confined dense CS shell in SN 2013fs (Yaron et al. 2017). This case produces a moderate interaction luminosity with the maximal contribution of about 18 per cent in the range of 2–7 d (Fig. 14a) that compensates a small deficit in the bolometric luminosity of the hydrodynamic model HM-optm at this stage (Fig. 9). Simultaneously, the CS interaction model meets the kinematic constraints imposed by the early He I 10 830 Å absorption and the NHVA of Hα and He I 10 830 Å (Fig. 14b).

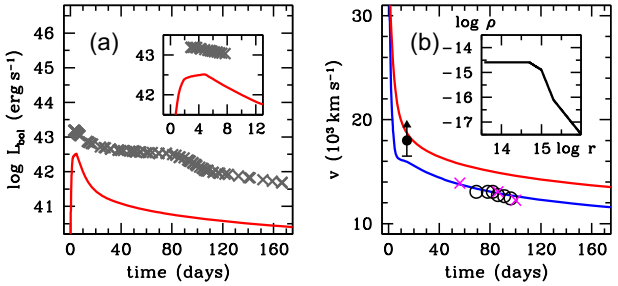

Figure 14. Observational effects of the CS interaction for the ejecta mass of 22 M$_\odot$ and the explosion energy of 6 $\times$ 10^{51} erg. The left-hand panel shows the computed bolometric luminosity due to only the CS interaction (red line) compared to the observed bolometric luminosity (grey crosses). The inset shows a zoom-in of the first 10 d that demonstrates a small contribution of the CS interaction to the SN luminosity at the stage $t < 2$ d. The right-hand panel shows the evolution of the CDS velocity (blue line) and the maximal velocity of the unshocked ejecta (red line). The filled circle corresponds to the lower limit of the maximal ejecta velocity inferred from the He I 10 830 Å absorption on day 14.48. Crosses correspond to the NHVA inferred from the Hα profile, while open circles are the NHVA inferred from the He I 10 830 Å line. Inset shows the corresponding CS density distribution.

The tension between the explosion energy of 6 $\times$ 10^{51} erg suggested by the CS interaction model and that of 10^{52} erg implied by the hydrodynamic model should not be considered as an irreducible one. Given the simplicity of the CS interaction model, this disparity indicates that the realistic hydrodynamic model should include the shock wave propagation in the CS shell, which however would require a more complex hydrodynamic approach in order to treat an essentially 3D physics related to the CDS formation and the Rayleigh–Taylor instability.

6 DISCUSSION AND CONCLUSIONS

The paper has been aimed at the study of the non-standard SN IIP 2017gmr with the emphasis on the unusual light curve at the plateau/tail transition and the steep tail decline. We find that a standard hydrodynamic model of the RSG star exploding with the ^{56}Ni ejecta is not able to describe the plateau/tail transition and the very tail for any model parameter set. In that sense we confirm the conclusion of Goldberg & Bildsten (2020), who demonstrate that their hydrodynamical model of SNe IIP fails to account for the plateau/tail transition and the luminosity tail of the SN 2017gmr light curve. The model with the high hydrogen abundance in the central zone of the ejecta and the high amount of ^{56}Ni is able to fit the light curve in the range of $t < 130$ d, although later on, the model tail is somewhat less steep compared to the observed one. Yet, this kind of

hydrodynamic model should be considered as a viable contender for the hydrodynamic model with the additional central energy source.

We find also that the light curve of SN 2017gmr can be reproduced in the framework of the FM-mechanism that implies a central energy source with the specific temporal behaviour of the power release. The extra energy source is attributed in this case to the fallback interaction with the magnetar in the propeller regime. This ad hoc scenario is in line with the extremely high explosion energy of $\approx 10^{52}$ erg and the bipolar ^{56}Ni asymmetry, both indicative of the magneto-rotational explosion. At the moment, we are not aware of other SNe IIP that would show similar behaviour of the bolometric light curve at the plateau/tail transition and the early stage of the luminosity tail. The another SN IIP that demonstrates a steep decline of the early tail is SN 2013ej (Dhungana et al. 2016). Although this behaviour has been explained in the model with the external ^{56}Ni (Utrobin & Chugai 2017), we do not rule out the FM-mechanism as a viable alternative. One should keep eye open on the possibility that the FM-mechanism could sometimes manifest itself at the radioactive tail of core-collapse SNe including SNe II varieties and SNe Ib/c.

The unusual bolometric light curve of SN 2017gmr raises a serious caveat. The point is that at the plateau/tail transition of SNe IIP the radiative cooling regime changes from the photospheric to the nebular one, which is accompanied by the corresponding spectrum transformation. This poses a question whether the technique for the bolometric flux reconstruction that is appropriate for the photospheric stage preserves the same accuracy at the nebular stage. The only case when we have no doubts in this regard is SN 1987A. In other cases of SNe IIP, some degree of doubt remains.

The hydrodynamic modelling confirms the earlier suggestion that the high luminosity and the fast expansion of the ejecta indicate the high explosion energy (Andrews et al. 2019). The explosion energy of 10^{52} erg inferred in our model is twice as large compared to 4.6×10^{51} erg, the value preferred by Goldberg & Bildsten (2020). Note, however, that the degeneracy of the light curves for SN 2017gmr admits also a model with the larger explosion energy of $\approx 10^{52}$ erg and, consequently, the ejecta mass larger than $22\,M_\odot$ (Goldberg & Bildsten 2020). Despite both hydrodynamic codes STELLA (Blinnikov et al. 1998; Blinnikov & Sorokina 2004; Baklanov, Blinnikov & Pavlyuk 2005; Blinnikov et al. 2006) used by Goldberg & Bildsten (2020) and our code CRAB (Utrobin 2004, 2007) produce the similar results for the normal SN IIP 1999em (Baklanov et al. 2005; Utrobin 2007), in the case of SN 2017gmr, some inconsistency is unavoidable because of the different adopted ^{56}Ni distribution and the different pre-SN configuration, namely evolutionary and non-evolutionary pre-SN models, respectively.

We have identified the NHVA in the Hα and He I 10 830 Å lines in the spectra between 50 and 100 d and use the velocities of these features to constrain the mass of the confined CS shell of $\sim 4 \times 10^{-3}\,M_\odot$, which turns out to be comparable to that of SN 2013fs (Yaron et al. 2017). The requirement of the low contribution of the CS interaction luminosity combined with the kinematic constraints from the NHVA implies the preferred explosion energy of 6×10^{51} erg that is lower than the energy implied by the hydrodynamic model. The contradiction casts a shadow on the thin shell model and suggests the need for the full radiation hydrodynamics treatment of the shock wave propagation in the dense CS shell, which however cannot be done by the available hydrodynamic code.

The explosion energy of SN 2017gmr is indeed enormous for SNe IIP and places this event to the category of high-energy SNe IIP with other two cases of SN 2000cb and SN 2009kf (Table 4, Fig. 15). The explosion energies of these three SNe exceed the upper limit for the neutrino-driven explosion mechanism that implies that their explosions could be related to the rotational energy of the collapsing core. Unfortunately, spectra of SN 2009kf and SN 2000cb at the late nebular stage are lacking, so one cannot say anything about possible asymmetry of the ^{56}Ni ejecta in these SNe. It is noteworthy that in both preferred models for SN 2017gmr, HM-hmix, and HP-optm (Table 1), the ^{56}Ni mass exceeds the amount of ^{56}Ni typical for SNe IIP (Table 4, Fig. 15), which is in line with the unusually high explosion energy of SN 2017gmr.

Table 4. Hydrodynamic models of SNe IIP.

SN	R_0 ($R_\odot$)	M_{ej} ($M_\odot$)	E (10^{51} erg)	M_{Ni} ($10^{-2}\,M_\odot$)	v_{Ni}^{max}	v_H^{min}
					(km s^{-1})	
1987A	35	18	1.5	7.65	3000	600
1999em	500	19	1.3	3.6	660	700
2000cb	35	22.3	4.4	8.3	8400	440
2003Z	230	14	0.245	0.63	535	360
2004et	1500	22.9	2.3	6.8	1000	300
2005cs	600	15.9	0.41	0.82	610	300
2008in	570	13.6	0.505	1.5	770	490
2009kf	2000	28.1	21.5	40.0	7700	410
2012A	715	13.1	0.525	1.16	710	400
2013ej	1500	26.1	1.4	3.9	6500	800
2016X	436	28.0	1.73	2.95	4000	760
2017gmr	525	22.0	10.2	11.0	3300	640

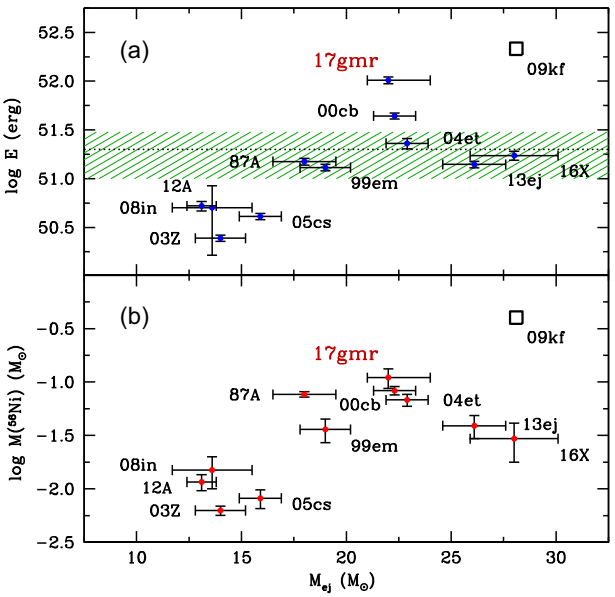

Figure 15. Explosion energy (panel a) and ^{56}Ni mass (panel b) versus ejecta mass for SN 2017gmr and 11 other core-collapse SNe (Utrobin & Chugai 2019). The dotted line in panel (a) is the upper limit of the explosion energy of 2×10^{51} erg for the neutrino-driven mechanism (Janka 2017) with the uncertainty of about $\pm 10^{51}$ erg[1] shown by the shaded green band.

ACKNOWLEDGEMENTS

VPU is partially supported by Russian Scientific Foundation grant 19-12-00229. This work makes use of observations from the Las Cumbres Observatory (LCO) global telescope network. The Las Cumbres Observatory team is supported by NSF grants AST-1911225 and AST-1911151.

DATA AVAILABILITY

The data underlying this paper will be shared on reasonable request to the corresponding author.

REFERENCES

Albareti F. D. et al., 2017, ApJS, 233, 25
Andrews J. E. et al., 2019, ApJ, 885, 43
Baklanov P. V., Blinnikov S. I., Pavlyuk N. N., 2005, Astron. Lett., 31, 429
Bisnovatyi-Kogan G. S., 1971, Sov. Ast., 14, 652
Blinnikov S., Sorokina E., 2004, Ap&SS, 290, 13
Blinnikov S. I., Eastman R., Bartunov O. S., Popolitov V. A., Woosley S. E., 1998, ApJ, 496, 454
Blinnikov S. I., Röpke F. K., Sorokina E. I., Gieseler M., Reinecke M., Travaglio C., Hillebrand t W., Stritzinger M., 2006, A&A, 453, 229
Brown T. M. et al., 2013, PASP, 125, 1031
Bullivant C. et al., 2018, MNRAS, 476, 1497
Burrows A., Vartanyan D., 2021, Nature, 589, 29
Catchpole R. M. et al., 1988, MNRAS, 231, 75P
Chevalier R. A., 1982, ApJ, 259, 302
Chevalier R. A., 1989, ApJ, 346, 847
Chugai N. N., 2001, MNRAS, 326, 1448
Chugai N. N., 2006, Astron. Lett., 32, 739
Chugai N. N., 2019, Astron. Lett., 45, 427
Chugai N. N., Danziger I. J., 1994, MNRAS, 268, 173
Chugai N. N., Fabrika S. N., Sholukhova O. N., Goranskij V. P., Abolmasov P. K., Vlasyuk V. V., 2005, Astron. Lett., 31, 792
Chugai N. N., Chevalier R. A., Utrobin V. P., 2007, ApJ, 662, 1136
Colgate S. A., 1971, ApJ, 163, 221
Colgate S. A., White R. H., 1966, ApJ, 143, 626
Dhungana G. et al., 2016, ApJ, 822, 6
Elmhamdi A. et al., 2003, MNRAS, 338, 939
Goldberg J. A., Bildsten L., 2020, ApJ, 895, L45
Grassberg E. K., Imshennik V. S., Nadyozhin D. K., 1971, Ap&SS, 10, 28
Illarionov A. F., Sunyaev R. A., 1975, Sov. Astron. Lett., 1, 73
Janka H.-T., 2017, in Alsabti A. W., Murdin P., eds, Neutrino-Driven Explosions, Springer International Publishing AG, Switzerland
Khokhlov A. M., Höflich P. A., Oran E. S., Wheeler J. C., Wang L., Chtchelkanova A. Y., 1999, ApJ, 524, L107
Kozma C., Fransson C., 1992, ApJ, 390, 602
LeBlanc J. M., Wilson J. R., 1970, ApJ, 161, 541
Liu W., Dalgarno A., 1995, ApJ, 454, 472
McCully C., Volgenau N. H., Harbeck D.-R., Lister T. A., Saunders E. S., Turner M. L., Siiverd R. J., Bowman M., 2018, in Guzman J. C., Ibsen J., eds, Proc. SPIE Conf. Ser. Vol. 10707, Software and Cyberinfrastructure for Astronomy V. SPIE, Bellingham, p. 107070K
MacFadyen A. I., Woosley S. E., Heger A., 2001, ApJ, 550, 410
Nagao T. et al., 2019, MNRAS, 489, L69
Nicholl M., 2018, Res. Notes AAS, 2, 230
Press W. H., Teukolsky S. A., Vetterling W. T., Flannery B. P., 2007, Numerical Recipes: The Art of Scientific Computing, 3rd edn. Cambridge Univ. Press, Cambridge
Shakura N. I., 1975, Sov. Astron. Lett., 1, 223
Shiode J. H., Quataert E., 2014, ApJ, 780, 96
Smith N. et al., 2012, MNRAS, 420, 1135
Smith N. et al., 2015, MNRAS, 449, 1876
Stetson P. B., 2000, PASP, 112, 925
Utrobin V. P., 2004, Astron. Lett., 30, 293
Utrobin V. P., 2007, A&A, 461, 233
Utrobin V. P., Chugai N. N., 2008, A&A, 491, 507
Utrobin V. P., Chugai N. N., 2011, A&A, 532, A100
Utrobin V. P., Chugai N. N., 2017, MNRAS, 472, 5004
Utrobin V. P., Chugai N. N., 2019, MNRAS, 490, 2042
Utrobin V. P., Chugai N. N., Botticella M. T., 2010, ApJ, 723, L89
Utrobin V. P., Wongwathanarat A., Janka H.-T., Müller E., 2017, ApJ, 846, 37
Valenti S. et al., 2016, MNRAS, 459, 3939
Weaver T. A., Woosley S. E., 1980, in Ehlers J., Perry J. J., Walker M., eds, Annals of the New York Academy of Sciences, Ninth Texas Symposium on Relativistic Astrophysics, Vol. 336, New York Academy of Sciences, New York, p. 335
Whitelock P. A. et al., 1988, MNRAS, 234, 5P
Woosley S. E., 1988, ApJ, 330, 218
Xu Y., McCray R., Oliva E., Rand ich S., 1992, ApJ, 386, 181
Yaron O. et al., 2017, Nat. Phys., 13, 510

This paper has been typeset from a TEX/LATEX file prepared by the author.